Journal of Theoretical Biology 487 (2020) 110107

Contents lists available at ScienceDirect

Journal of Theoretical Biology

journal homepage: www.elsevier.com/locate/jtb

Electric potential generation of electrocytes: Modelling, analysis, and computation

Xiulei Cao[a], Zilong Song[a], Tzyy-Leng Horng[b,c], Huaxiong Huang[a,d,e,*]

[a] Department of Mathematics and Statistics, York University, Toronto, Canada
[b] Department of Applied Mathematics, Feng Chia University, Taichung 40724, Taiwan
[c] National Center for Theoretical Sciences, Taipei Office, Taipei 10617, Taiwan
[d] BNU-UIC Joint Mathematical Research Centre, Zhuhai, China
[e] Department of Computer Science, University of Toronto, Toronto, Canada

ARTICLE INFO

Article history:
Received 13 July 2019
Revised 30 November 2019
Accepted 5 December 2019
Available online 10 December 2019

Keywords:
Electrocyte
Poisson–Nernst–Planck system
Asymptotic analysis
Numerical simulation
Voltage generation

ABSTRACT

In this paper, we developed a one-dimensional model for electric potential generation of electrocytes in electric eels. The model is based on the Poisson–Nernst–Planck system for ion transport coupled with membrane fluxes including the Hodgkin–Huxley type. Using asymptotic analysis, we derived a simplified zero-dimensional model, which we denote as the membrane model in this paper, as a leading order approximation. Our analysis provides justification for the assumption in membrane models that electric potential is constant in the intracellular space. This is essential to explain the superposition of two membrane potentials that leads to a significant transcellular potential. Numerical simulations are also carried out to support our analytical findings.

1. Introduction

Electric eels (*electrophorus electricus*) have interested scientists for centuries. Electric discharge was discovered by scientists in late 1700s, and was generated by an identifiable electric organ (Markham, 2013). The high-voltage electric discharge is used to stun prey or defend themselves from predators (Nelson et al., 2016), while high-frequency or low-intensity discharges are used for active sensing and communication (Catania, 2015a; Lissmann, 1958). The electric organ has several thousands of electrogenic cells, called electrocytes, stacked in series. Each electrocyte produces a potential difference of 0.15 V, but stacked electrocytes can generate a huge voltage similar to stacked plates in a battery (Gotter et al., 1998; Mauro, 1969).

Electrocytes work much like muscle or nerve cells. The mechanism of voltage generation is associated with the membrane potentials and ionic fluxes (currents) across the membranes of electrocyte. There is an ion concentration gradient across membrane, which maintains an equilibrium membrane potential at resting state (approximately −85 mV for electrocyte). Electrocyte possesses two primary membranes: the innervated membrane and the non-innervated membrane (Gotter et al., 1998; Xu and Lavan, 2008), where various types of transmembrane proteins (such as ion channels and pumps) abound and work in synergy to generate unusual phenomenon or fulfil a function. Like in nerve cells, action potential (AP) can be triggered at the innervated membrane, which in turn causes a difference in electric potential (0.15V). Such mechanism has been utilized to design synthetic cells, aiming to convert ion concentration gradient to APs, which has potential applications for powering medical implants (Humayun et al., 2003; Xu and Lavan, 2008).

Since the 1950s, many experiments have been conducted to investigate the electrogenic mechanisms and the functions of electric discharge with different intensity or frequency. It was reported that (Brown, 1950; Coates, 1950) high-voltage discharge produced by eels can be as high as 600 V and the external current can be up to 1 A. Recently, Catania (2015b) showed that the high-voltage discharge with high frequency can be used to track fast-moving prey and guide the strike, similar to the “terminal feeding buzz” of bats. He also investigated the electromotive force and internal resistance for discharge during the defensive leaping behavior (Catania, 2017a; 2017b), by an equivalent circuit. In addition, there have been many investigations on voltage-gated channels, AP, and waveforms of discharge of electrocytes (Dunlap et al., 1997; Gotter et al., 1998; Noda et al., 1984). For more experimental

* Corresponding author.
E-mail addresses: hhuang@uic.edu.hk, hhuang@mathstat.yorku.ca (H. Huang).

https://doi.org/10.1016/j.jtbi.2019.110107
0022-5193/

studies, see also Keynes and Martins-Ferreira (1953); Markham (2013); Sheridan and Lester (1977).

Many mathematical models can describe various ion transport through ion channels, including the famous Hodgkin–Huxley (HH) model (Hodgkin and Huxley, 1990) and Goldman–Hodgkin–Katz (GHK) model (Hille et al., 2001). The HH model has been used to show AP in squid giant axon (Hodgkin and Huxley, 1952; George et al., 2015), but could not be directly applied to the electrocyte due to cell polarity. In the HH model for squid axon, all types of ion channels are assumed to be distributed uniformly on the circumferential membrane. The membrane potential to be computed in HH model is the difference between intracellular and extracellular electric potential. Basically, intracellular and extracellular potentials are assumed to be constants in space, and the HH model is an ODE or membrane model unable to accommodate the boundary layer (BL, electric double layer) of the membrane.

In Xu and Lavan's membrane model (Xu and Lavan, 2008), various types of ion channels and pumps (Altamirano, 1955; Gotter et al., 1998; Keynes and Martins-Ferreira, 1953) are assumed to be distributed on innervated and non-innervated membranes respectively. The electric potentials in and outside the electrocyte are assumed to be constants as in the HH model for squid axon. However, there is a crucial difference between the two cases since the two extracellular domains next to the innervated and non-innervated membranes are separated, while the extracellular domain in the HH model for squid axon is connected. This was not addressed in Xu and Lavan (2008) and the innervated and non-innervated membrane potentials were computed using two independent ODEs. It was shown that the innervated membrane is depolarized from -85 mV to 65 mV before re-polarizing and return to the resting state. For the non-innervated membrane, it was implied that the potential remains at its resting state regardless the changes at the innervated membrane. These two membrane potentials are superposed to obtain the transcellular potential up to 150 mV. The total potential of the electric organ can be obtained by summing the transcellular potentials of electrocytes since they are placed in series. This superposition principle is valid provided that the electric potential does not vary in the intracellular domain, except in the BLs next to the innervated and non-innervated membranes. These issues provide the main motivation for exploring the dynamics of a model electrocyte through a PDE approach since they can not be addressed by the membrane model in Xu and Lavan (2008), which does not allow for spatial variations of electric potential inside each of the three domains (one intracellular and two extracellular domains).

In this paper, we investigate the mechanism of electric potential generation of electrocytes in the case of an open circuit. We start with a more fundamental model for ion transport in biological systems. The model consists of electro-diffusion (Nernst-Planck) equation for major ion species such as sodium, potassium and chloride, and a Poisson equation for the electricity field. This Poisson-Nernst-Planck (PNP) system has been successfully applied to model ion transport in cells and ion channels (Liu, 2009; Rubinstein, 1990; Mori et al., 2011; Kenny et al., 2018; Gardner and Jones, 2011), as well as AP propagation in axons when coupled with the HH membrane fluxes (Pods et al., 2013; Song et al., 2018a; 2018b). Using asymptotic analysis, we have derived a membrane model from our PNP model, which is consistent with the one in Xu and Lavan (2008). Our analysis provides the justification of the assumptions made in Xu and Lavan (2008). In the leading approximation, the electric potential in the bulk of intra/extra-cellular regions holds uniform, and the membrane can be treated as a capacitor with effective charges stored in BLs.

The rest of the paper is structured as follows. The complete formulation with PNP system and general ionic flux models through membranes is given in Section 2. The non-dimensionalization is conducted in Section 3. Section 4 studies important features of the PNP system by asymptotic analysis, and the membrane model is derived. In Section 5, specific flux models are adopted and detailed numerical simulations are carried out to illustrate the mechanism of potential generation and to verify other features in analysis. Finally, we summarize our findings and comment on a follow up project with a closed circuit.

2. Problem formulation

Fig. 1 (a) illustrates the two-dimensional (2D) view of stacked electrocytes. The transmembrane proteins in the electrocytes are asymmetrically distributed across two primary membranes (Keynes and Martins-Ferreira, 1953; Gotter et al., 1998), one innervated and the other non-innervated. As the high voltage generated by electric eel's electric organ is a superposition of the difference in electric potential generated by electrocyte in series, we concentrate on a unit structure of electrocyte, illustrated in Fig. 1(b). For simplicity, we treat the electrocyte as a one-dimensional structure, with one intracellular (IC) region in the middle and two extracellular (EC) regions on two sides. Let a and b denote respectively the positions of innervated and non-innervated membranes.

Poisson-Nernst-Planck (PNP) system is often used to describe the transport of ions in cells. It is derived by treating ions as point charges and provides a very good approximation for dilute ionic solutions (Kilic et al., 2007a; 2007b; Song et al., 2019) as in the extracellular and intracellular regions here (the relative error is of order 10^{-3} by estimate from steric PNP models). Ionic currents (or fluxes) through membrane are given by various experimental or empirical models, depending on the types of ion channels involved. The general forms of the currents are presented here, and the specific examples are given in Section 5.1 to show the numerical results.

In this paper, we focus on three ion species Na^+, K^+ and Cl^- as in Fig. 1, since they are the three major ions (sometimes called bio-ions) most relevant for generating electric pulses in electrcytes. Let c_i $(i = 1, 2, 3)$ denote concentrations of Na^+, K^+ and Cl^-, with valences $z_1 = z_2 = 1$, $z_3 = -1$. The one-dimensional PNP system is

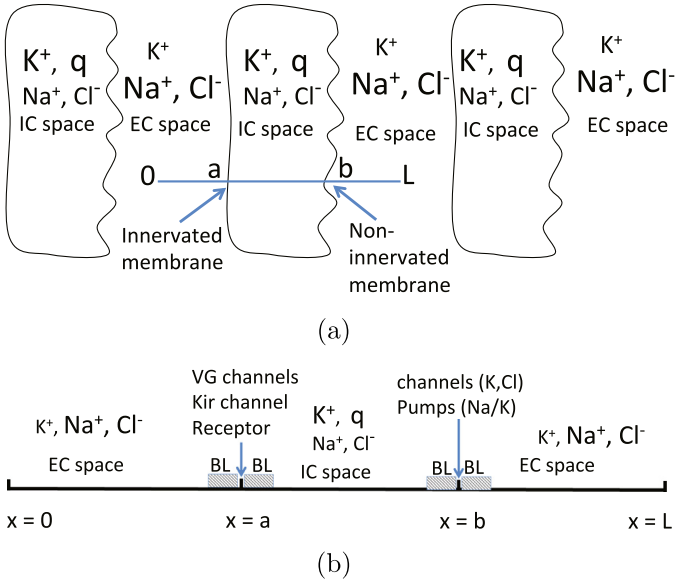

Fig. 1. (a) Two-dimensional view of stacked electrocytes, where EC and IC stand for extracellular and intracellular respectively, (b) the one-dimensional setup of unit structure of electrocyte, where VG stands for voltage-gated.

given by Rubinstein (1990); Song et al. (2018b)

$$-\epsilon_0\epsilon_r\partial_{xx}\psi = e_0N_A\left(\sum_{i=1}^{3} z_ic_i + q\right), \quad x \in (0,a)\cup(a,b)\cup(b,L), \tag{1}$$

$$\partial_t c_i = -\partial_x J_i, \quad J_i = -D_i\left(\partial_x c_i + \frac{z_i e_0}{k_B T}c_i\partial_x\psi\right), \quad i = 1,2,3, \tag{2}$$

where the first (Poisson) and the second (Nernst–Planck) equations govern the electrostatic potential $\psi(x, t)$ and ionic concentration $c_i(x, t)$, respectively. There is negative fixed charge q in the intracellular region, while $q = 0$ in the extracellular regions. The ionic fluxes J_i $(i = 1, 2, 3)$ consist of two parts, due to the ionic concentration gradient and the electric field, and D_i $(i = 1, 2, 3)$ are the diffusion constants. Other parameters (given in Appendix B) are vacuum permittivity ϵ_0, relative permittivity ϵ_r, elementary charge e_0, Avogadro constant N_A, Boltzmann constant k_B, and absolute temperature T.

The left membrane $x = a$ corresponds to the innervated membrane of electrocyte. On this membrane, there are voltage-gated channels (Bezanilla, 2007; Malmivuo and Plonsey, 1995; Hodgkin and Huxley, 1990), inward rectifier K^+ channels (Kir) (Nygren et al., 1998), and acetylcholine receptors (AChRs) (Adams, 1981). The membrane currents are assigned as positive if they are from intracellular region to extracellular region. The current through voltage-gated channels is given by

$$I_i^{VG} = I_i^{VG}(V_m^a, c_{i,+}^a, c_{i,-}^a; \theta), \quad i = 1,2,3, \tag{3}$$

where $V_m^a = \psi_+^a - \psi_-^a$ is the membrane potential at membrane $x = a$, and θ represents the gating variable(s), whose dynamics depends on V_m. Hereafter, superscripts a and b mean the innervated and non-innervated membranes at $x = a$ and $x = b$, and $\pm$ denote the right and left limits of quantities on the membrane. Although the concentrations of other ions are not explicitly shown in the formula (3) of ion species i, their effects are reflected in the membrane potential V_m^a which is determined by all ions.

Additional current from rectifier K^+ channel (Kir channel) takes the form Nygren et al. (1998); Xu and Lavan (2008)

$$I_2^{Kir} = I_2^{Kir}(V_m^a, c_{2,+}^a, c_{2,-}^a). \tag{4}$$

This channel is specific for K^+ and the conductance is considered to be a constant, which is different from the voltage gated channels discussed earlier.

The stimulus current is generated by special receptors, which are open when two agonists, such as acetylcholine ACh, bind with them Mitra et al. (2005); Xu and Lavan (2008). The chemical binding process is described by an allosteric kinetic model (Chakrapani et al., 2004; Adams, 1981)

$$2A + R \underset{k_{-1}}{\overset{2k_{+1}}{\rightleftharpoons}} A + AR \underset{2k_{-2}}{\overset{k_{+2}}{\rightleftharpoons}} A_2R, \tag{5}$$

where R and A denote the receptor and the agonist, k_{+1}, k_{-1}, k_{+2} and k_{-2} are the association and dissociation rate constants of the binding processes. The rate constants $k_{\pm1}$, $k_{\pm2}$ are assumed to be constant independent of concentrations, and are often determined experimentally. In general, the ACh receptor is not selective and allows currents of many cations (Adams, 1981). This is the main mechanism to induce extra current initially to disturb the equilibrium state, which is necessary to trigger AP later controlled by voltage-gated channels. The extra current through these receptors will gradually decay to 0. The general forms for the currents of Na^+ and K^+ through the receptor are written as

$$I_i^R = I_i^R(V_m^a, [A], k_{\pm1}, k_{\pm2}, t), \quad i = 1,2, \tag{6}$$

where [A] is the concentration of the agonist. As it is the total current $I_1^R + I_2^R$ that is determined experimentally, we will compare several combinations with the same total current in numerical simulations in Section 5. The effects of concentrations are reflected in the membrane potential V_m^a.

At $x = b$ is the non-innervated membrane of electrocyte, where there are both channels (K^+ and Cl^-) and pumps (Na^+/K^+). The general forms for the currents through the channels are denoted by

$$I_1^b = 0, \quad I_i^b = I_i^b(V_m^b, c_{i,-}^b, c_{i,+}^b), \quad i = 2,3, \tag{7}$$

where $V_m^b = \psi_-^b - \psi_+^b$ is the membrane potential at membrane $x = b$. Since there are no Na^+ channels on this membrane, Na^+ current is set to be 0. These channels have constant conductance (not voltage-gated), and will react to the changes in electrical potentials induced by the other innervated membrane. The currents through the pumps are Goldshlegger et al. (1987); Novotny and Jakobsson (1996)

$$I_i^{pump} = I_i^{pump}(V_m^b, c_{1,-}^b, c_{1,+}^b, c_{2,-}^b, c_{2,+}^b), \quad i = 1,2, \quad I_3^{pump} = 0. \tag{8}$$

The pumps are responsible to recover and maintain equilibrium concentrations.

These currents provide the flux conditions at the two membranes for the PNP system

$$\begin{aligned} -z_1e_0N_AJ_1 &= I_1^{VG} + I_1^R, && \text{at} \quad x = a,\\ -z_2e_0N_AJ_2 &= I_2^{VG} + I_2^R + I_2^{Kir}, && \text{at} \quad x = a,\\ -z_3e_0N_AJ_3 &= I_3^{VG}, && \text{at} \quad x = a,\\ z_ie_0N_AJ_i &= I_i^b + I_i^{pump}, \qquad i = 1,2,3, && \text{at} \quad x = b. \end{aligned} \tag{9}$$

Two conditions for ψ are also needed on each membrane. Assume that the membranes have thickness h_m and relative permittivity ϵ_r^m, and with a constant electric field. Thus, the electric potential is linear inside both membranes, which implies

$$\epsilon_r\partial_x\psi|_{x=a\pm} = \epsilon_r^m\frac{\psi_+^a - \psi_-^a}{h_m}, \quad \epsilon_r\partial_x\psi|_{x=b\pm} = \epsilon_r^m\frac{\psi_+^b - \psi_-^b}{h_m}, \tag{10}$$

where $a\pm$ and $b\pm$ denote the left and right limits at $x = a$ and b.

We use typical bulk concentrations (Gotter et al., 1998) under electro-neutrality as the initial values at $t = 0$

$$\begin{aligned} &c_1(x,0) = 160\,\text{mM}, \quad c_2(x,0) = 2.5\,\text{mM}, \quad c_3(x,0) = 162.5\,\text{mM},\\ &\quad \text{for} \quad 0 < x < a \text{ and } b < x < L\\ &c_1(x,0) = 8.928\,\text{mM}, \quad c_2(x,0) = 72.048\,\text{mM}, \quad c_3(x,0) = 9.328\,\text{mM},\\ &\quad \text{for} \quad a < x < b. \end{aligned} \tag{11}$$

For the boundary conditions at $x = 0$ and L, we have

$$\begin{aligned} &\psi(0,t) = 0, \quad c_1(0,t) = 160\,\text{mM}, \quad c_2(0,t) = 2.5\,\text{mM},\\ &\quad c_3(0,t) = 162.5\,\text{mM},\\ &\frac{\partial\psi}{\partial x}(L,t) = 0, \quad c_1(L,t) = 160\,\text{mM}, \quad c_2(L,t) = 2.5\,\text{mM},\\ &\quad c_3(L,t) = 162.5\,\text{mM}. \end{aligned} \tag{12}$$

Note that ψ needs to be fixed at one position to ensure a unique solution, and it is set to be zero on the left boundary ($x = 0$) without loss of generality. It will be equivalent by fixing a value on the right boundary or at a middle point.

3. Non-dimensionalisation

In this section, we present dimensionless system for the preceding formulation, which will be used in analysis and simulation. We adopt the following scalings

$$\begin{aligned} &\tilde\psi = \frac{\psi}{k_BT/e_0}, \quad \tilde c_i = \frac{c_i}{c_0}, \quad \tilde q = \frac{q}{c_0}, \quad \tilde D_i = \frac{D_i}{D_0}, \quad \tilde t = \frac{t}{L^2/D_0},\\ &\tilde x = \frac{x}{L}, \quad \tilde h_m = \frac{h_m}{L}, \quad \tilde a = \frac{a}{L}, \quad \tilde b = \frac{b}{L}, \quad \tilde J_i = \frac{J_i}{D_0c_0/L}, \end{aligned} \tag{13}$$

where c_0 is the extracellular bulk concentration of Na^+, D_0 is typical diffusion constant, L is the total length of unit structure, and the diffusion time scale is adopted. The currents I_i on the right-hand side of (9) and the associated conductances and permeabilities therein are scaled respectively by

$$I_0 = \frac{c_0 D_0 e_0 N_A}{L}, \quad G_0 = \frac{c_0 D_0 e_0^2 N_A}{k_B T L}, \quad P_0 = \frac{D_0}{L}. \tag{14}$$

The values of the above quantities in scaling are given in Appendix B.

In the following, we remove the tilde for simplicity, and use the same notations for the dimensionless quantities. For intracellular and extracellular regions, the dimensionless PNP system is given by

$$\begin{aligned} &-\epsilon^2 \partial_{xx}\psi = \sum_{k=1}^{3} z_k c_k + q, \quad x \in (0,a)\cup(a,b)\cup(b,1), \\ &\partial_t c_i = -\partial_x J_i = D_i \partial_x(\partial_x c_i + z_i c_i \partial_x \psi), \quad i = 1,2,3, \end{aligned} \tag{15}$$

where we have $q = -0.4478$ for $a < x < b$ and $q = 0$ for the other regions. The parameter ϵ is defined by

$$\epsilon = \frac{\lambda_D}{L}, \quad \lambda_D = \sqrt{\frac{\epsilon_0 \epsilon_r k_B T}{e_0^2 N_A c_0}}, \tag{16}$$

where λ_D is the Debye length.

At the membranes, we have the flux conditions

$$\begin{aligned} -z_1 J_1 &= I_1^{VG} + I_1^R, && \text{at} \quad x = a, \\ -z_2 J_2 &= I_2^{VG} + + I_2^R + I_2^{Kir}, && \text{at} \quad x = a, \\ -z_3 J_3 &= I_3^{VG}, && \text{at} \quad x = a, \\ z_i J_i &= I_i^b + I_i^{pump}, \quad i = 1,2,3, && \text{at} \quad x = b. \end{aligned} \tag{17}$$

The interface conditions at membranes for ψ become

$$\epsilon^2 \partial_x \psi\big|_{x=a\pm} = \epsilon_m^2 \frac{\psi_+^a - \psi_-^a}{h_m}, \quad \epsilon^2 \partial_x \psi\big|_{x=b\pm} = \epsilon_m^2 \frac{\psi_+^b - \psi_-^b}{h_m}, \tag{18}$$

where

$$\epsilon_m = \sqrt{\frac{\epsilon_0 \epsilon_r^m k_B T}{e_0^2 N_A c_0 L^2}}. \tag{19}$$

All the dimensionless parameters are given in Appendix C.

The dimensionless initial values at $t = 0$ are given by

$$\begin{aligned} &c_1(x,0) = 1, \quad c_2(x,0) = 0.0156, \quad c_3(x,0) = 1.0156, \\ &\quad \text{for} \quad 0 < x < a \text{ and } b < x < 1, \\ &c_1(x,0) = 0.0558, \quad c_2(x,0) = 0.4503, \quad c_3(x,0) = 0.0583, \\ &\quad \text{for} \quad a < x < b. \end{aligned} \tag{20}$$

For the boundary conditions at $x = 0$ and 1, we have

$$\begin{aligned} &\psi(0,t) = 0, \quad c_1(0,t) = 1, \quad c_2(0,t) = 0.0156, \\ &\quad c_3(0,t) = 1.0156, \\ &\tfrac{\partial \psi}{\partial x}(1,t) = 0, \quad c_1(1,t) = 1, \quad c_2(1,t) = 0.0156, \\ &\quad c_3(1,t) = 1.0156. \end{aligned} \tag{21}$$

4. Asymptotic analysis

There have been attempts to study the high-voltage discharge using membrane models (Xu and Lavan, 2008) with some assumptions (i.e., electric potential and concentrations are uniform in bulk EC and IC regions). In the previous section, we have formulated the problem with a more fundamental PNP model, with no extra assumptions. This section aims to use asymptotic analysis to derive a leading order membrane model and examine the validity of the assumptions. Firstly, note that there exist BLs next to both membranes due to the fact that ϵ is small. In addition, there is a separation in scales between the membrane dynamics and the transport of ions in the EC and IC regions outside the BLs. As a consequence, the spatial distribution of electric potential ψ and concentrations c_i $(i = 1,2,3)$ can be approximated by piecewise constants in the bulk of the EC and IC regions and membrane potential V_m^b remains as a constant.

4.1. Constant ψ in the bulk regions

In this subsection, we conduct asymptotic analysis to show that ψ is almost constant in each bulk of the three regions. From experiments and simulations as well as the estimate by the parameter values, the relevant time scale for AP generation in electrocytes is milliseconds, which is mainly controlled by the time scale of the receptor (e.g., the parameter α_0 in (55)) and dynamics of gating variable θ (e.g., n, m, h in Appendix A). It is much smaller than the diffusion time scale (estimated at the order of 10 s). Therefore, the ratio of the two time scales is roughly the same order of $\epsilon \sim 10^{-5}$, and we adopt a new time scale in the following analysis

$$\hat{t} = \frac{t}{t_0}, \quad t_0 = \epsilon \frac{L^2}{D_0} = \frac{L\lambda_D}{D_0}. \tag{22}$$

Then, the dimensionless equation for c_i in (15) will become

$$\partial_{\hat{t}} c_i = -\epsilon \partial_x J_i = \epsilon D_i \partial_x(\partial_x c_i + z_i c_i \partial_x \psi), \quad i = 1,2,3, \tag{23}$$

then $\hat{t} \sim O(1)$ is of interest.

It is well known that there are BLs of thickness $O(\epsilon)$ near the membrane (cf. Fig. 1(b)), under normal physiological conditions. There have been a number of BL analyses for the PNP system, and interested readers can find more details in Song et al. (2018b). In this paper, we focus on the solution in the bulk regions away from the BLs. Hereafter, we use "bulk" to mean the bulk/inner region of associated interval away from the BL near membrane. In bulk, all the concerned quantities are at most $O(1)$ and taking the derivative $\partial_{\hat{t}}$ or ∂_x will not increase the order since there is no internal layer in bulk. In other words, we get

$$\begin{aligned} &\psi, \partial_x \psi, \ldots, = O(1), \quad c_i, \partial_x c_i, \ldots, = O(1), \quad J_i, \partial_x J_i, \ldots, = O(1), \\ &\quad i = 1,2,3. \end{aligned} \tag{24}$$

By (23), (24), the variation of c_i in bulk is at most $O(\epsilon)$, and we conclude that c_i is constant at leading order in the bulk. Taking the derivative ∂_x on (23) gives

$$\partial_{\hat{t}}(\partial_x c_i) = -\epsilon \partial_{xx} J_i = O(\epsilon), \quad i = 1,2,3. \tag{25}$$

With initial condition $\partial_x c_i = 0$ at $\hat{t} = 0$, we have $\partial_x c_i(x,\hat{t}) = O(\epsilon)$, $i = 1,2,3$, in bulk. As a result, to leading order the flux in the bulk is dominated by the drift term from electric field

$$J_i = -D_i z_i c_i \partial_x \psi + O(\epsilon), \quad i = 1,2,3. \tag{26}$$

By $(15)_1$, we obtain the electro-neutral (EN) condition $\sum_{i=1}^{3} z_i c_i + q = O(\epsilon^2)$ in bulk. Then, multiplying z_i in (23) and summing up lead to

$$-\epsilon \partial_x \left(\sum_{i=1}^{3} z_i J_i \right) = \partial_{\hat{t}} \left(\sum_{i=1}^{3} z_i c_i \right) = \partial_{\hat{t}} \left(\sum_{i=1}^{3} z_i c_i + q \right) = O(\epsilon^2). \tag{27}$$

This means that the variation of total ionic current in bulk is small

$$-\partial_x \left(\sum_{i=1}^{3} z_i J_i \right) = O(\epsilon). \tag{28}$$

Note that this does not mean that each individual flux across the membrane is small, and numerical results show that it can be significant. However, the total current is small and the excessive charge mainly stays in BL as a capacitor.

We start with the bulk region of $(b, 1)$. Combining (26) and (28), and using the fact that $\partial_x c_i = O(\epsilon)$, at the leading order we have

$$\left(\sum_{i=1}^{3} z_i^2 D_i c_i \right) \partial_{xx} \psi = 0 \quad \Rightarrow \quad \partial_x \psi = \text{constant}. \tag{29}$$

Using the boundary condition $\partial_x\psi = 0$ at $x = b$, we obtain $\partial_x\psi = 0$ and hence ψ is a constant throughout the bulk of $(b, 1]$.

Next we examine the bulk region of (a, b). By (26) and the fact $\partial_x\psi = 0$ in the bulk of $(b, 1)$, at leading order we have

$$\sum_{i=1}^{3} z_i J_{iR}^b = 0, \tag{30}$$

where J_{iR}^b is the right limit of bulk flux at $x = b$. Hereafter, subscripts L and R denote the left and right limits of bulk quantities at membranes. Using the results in Song et al. (2018b), at leading order we have

$$\epsilon J_i^b = -z_i(\epsilon J_{iR}^b + \epsilon\,\partial_t F_{iR}) = -z_i(\epsilon J_{iL}^b - \epsilon\,\partial_t F_{iL}), \quad i = 1, 2, 3, \tag{31}$$

where J_{iL}^b is the left limit at $x = b$ from bulk flux in the region (a, b), and the expressions of F_{iR} and F_{iL} are given in Appendix C. After multiplying z_i to (31) and summing up, we have

$$\epsilon\sum_{i=1}^{3} z_i J_{iL}^b = \epsilon\sum_{i=1}^{3} z_i J_{iR}^b + \partial_{\hat{t}}\left(\epsilon\sum_{i=1}^{3} z_i F_{iR}\right) + \partial_{\hat{t}}\left(\epsilon\sum_{i=1}^{3} z_i F_{iL}\right). \tag{32}$$

For the present case, it is easy to prove as in Song et al. (2018b) that at leading order

$$\partial_{\hat{t}}\left(\epsilon\sum_{i=1}^{3} z_i F_{iR}\right) = C_m\partial_{\hat{t}}V_m^b = -\partial_{\hat{t}}\left(\epsilon\sum_{i=1}^{3} z_i F_{iL}\right), \tag{33}$$

where $C_m = \epsilon_m^2/h_m$ is the membrane capacitance. Physically, the two terms in brackets denote the excessive charge at leading order (see also $\sum z_i Q_{b^{\pm},i}$ in (41)). Therefore, combining (30), (32) and (33) and taking out the factor ϵ lead to

$$\sum_{i=1}^{3} z_i J_{iL}^b = 0, \tag{34}$$

which means the total current to the bulk of (a, b) is 0 at leading order. Eqs. (28) and (34) imply

$$\sum_{i=1}^{3} z_i J_i = 0, \quad \text{in the bulk of } (a, b), \tag{35}$$

and hence by (26)

$$\sum_{i=1}^{3} z_i J_i = -\left(\sum_{i=1}^{3} D_i z_i^2 c_i\right)\partial_x\psi = 0, \quad \Rightarrow \quad \partial_x\psi = 0, \tag{36}$$

holds in the bulk of (a, b). Thus, ψ is a constant in the bulk of (a, b).

Finally for the interval $(0, a)$, we can apply a similar argument at the membrane $x = a$ and conclude that the current in the bulk of $(0, a)$ is 0 at leading order and hence that $\partial_x\psi = 0$. Therefore, we obtain $\psi = 0$ at leading order by using boundary condition $\psi(0, t) = 0$ in (21).

4.2. Derivation of the membrane model

In this subsection, we derive a leading-order membrane model from the PNP model, which is consistent with that in Xu and Lavan (2008). We also show that the membrane potential V_m^b at the non-innervated membrane does not vary during the depolarization and repolarization phases of V_m^a.

We take the membrane $x = b$ for illustration. Using (30), (31), and (33), we have

$$C_m\partial_{\hat{t}}V_m^b = \epsilon\,\partial_{\hat{t}}\left(\sum_{i=1}^{3} z_i F_{iR}\right) = -\epsilon\sum_{i=1}^{3} z_i J_i^b = -\epsilon\sum_{i=1}^{3}(I_i^b + I_i^{pump}), \tag{37}$$

where we have also used interface condition $(17)_4$ in the last equality. The factor ϵ is present here because we have adopted a fast time scale. In fact, there are different ways to derive Eq. (37), and they are asymptotically equivalent to that in Song et al. (2018b). To provide more physical insight, we start from the original system in Section 3. Integrating $(15)_1$ from b to 1, we get

$$\epsilon^2\partial_x\psi(b) = \epsilon^2(\partial_x\psi(b) - \partial_x\psi(1)) = \int_b^1\sum_{i=1}^{3} z_i c_i dx, \tag{38}$$

where the argument t is omitted in the derivation for simplicity. By using membrane condition (18), Eq. (38) becomes

$$-C_m V_m^b = \int_b^1\sum_{i=1}^{3} z_i c_i dx. \tag{39}$$

Taking the time derivative in diffusion time scale and using equation $(15)_2$, we get (i.e., (37) without ϵ)

$$\begin{aligned} C_m\partial_t V_m^b &= -\int_b^1\sum_{i=1}^{3} z_i\partial_t c_i dx = \int_b^1\sum_{i=1}^{3} z_i\partial_x J_i dx \\ &= \sum_{i=1}^{3} z_i(J_i(1) - J_i(b)) = -\sum_{i=1}^{3}(I_i^b + I_i^{pump}). \end{aligned} \tag{40}$$

In the last equality we have used membrane condition $(17)_4$ and the fact that the current at $x = 1$ is asymptotically 0.

Remark. By (39), the membrane can be interpreted as a capacitor. We define the excessive charge for each ionic species at two sides of the non-innervated membrane as

$$Q_{b^-,i} = \int_{0.5}^{b} c_i(x) - c_i(0.5)dx, \quad Q_{b^+,i} = \int_b^1 c_i(x) - c_i(1)dx, \quad i = 1, 2, 3. \tag{41}$$

Using electro-neutral condition $\sum_{i=1}^{3} z_i c_i(1) = 0$, we can rewrite (39) as

$$-C_m V_m^b = \int_b^1\sum_{i=1}^{3} z_i(c_i - c_i(1))dx = \sum_{i=1}^{3} z_i Q_{b^+,i}. \tag{42}$$

Similarly, if we apply the condition (36) in the bulk of intracellular region, e.g., $x = 0.5$, we obtain

$$C_m V_m^b = \int_{0.5}^{b}\sum_{i=1}^{3} z_i(c_i - c_i(0.5))dx = \sum_{i=1}^{3} z_i Q_{b^-,i}. \tag{43}$$

Eqs. (42) and (43) indicate that the membrane at $x = b$ can be modelled as a capacitor, whose effective charge on each side is the excessive charge mainly stored in BL near membrane.

Following a similar procedure or using the analysis in Section 4.1, we obtain the dynamic equation for V_m^a

$$C_m\partial_t V_m^a = \sum_{i=1}^{3} z_i J_i^a = -\left(I_1^{VG} + I_1^R + I_2^{VG} + I_2^R + I_2^{Kir} + I_3^{VG}\right). \tag{44}$$

These two Eqs. (40) and (44) for the two membrane potentials have similar forms as the membrane model (Xu and Lavan, 2008), except that V_m^a and V_m^b and the variables appearing in the formulas of currents are interpreted as bulk quantities in the membrane model. We take (40) as an example to illustrate that it is a leading order approximation. It is clear from estimates in Song et al. (2018b) and numerical simulation in the next section that the variation of ψ in BL is small compared with V_m^b, and we have

$$\psi_L^b - \psi_-^b,\ \psi_R^b - \psi_+^b \sim O(\epsilon\,\partial_x\psi(b)) \sim O\left(\frac{\epsilon_m^2}{\epsilon h_m}\right) \sim 10^{-2}, \tag{45}$$

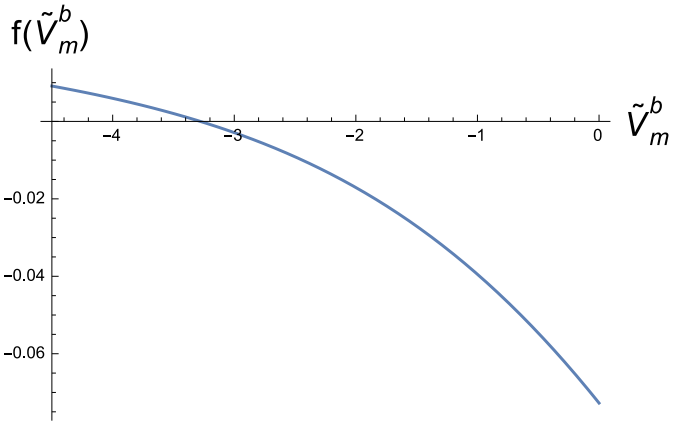

Fig. 2. The function $f(\tilde{V}_m^b)$ with specific formulas of currents in Section 5.1.

where the first $\sim$ is based on the asymptotic analysis (Song et al., 2018b) and the second $\sim$ is from interface condition $(18)_2$. Thus, we can replace V_m^b by the bulk values

$$V_m^b = \psi_-^b - \psi_+^b \approx \tilde{V}_m^b = \psi_L^b - \psi_R^b. \tag{46}$$

Estimates of (45) and (46) are also given in Appendix D in a slightly different way. Similarly, we replace $c_{i,+}^b, c_{i,-}^b$ by bulk concentrations $c_{i,R}^b, c_{i,L}^b$ as leading-order approximations in the formulas of currents, based on continuity of electro-chemical potential across the BL and similar estimates as in (45) (Song et al., 2018b). Therefore, (40) can be rewritten as

$$C_m \frac{d}{dt}\tilde{V}_m^b = f(\tilde{V}_m^b) = -\tilde{I}_2^b - \tilde{I}_3^b - \tilde{I}_1^{pump} - \tilde{I}_2^{pump}, \tag{47}$$

where we have defined from (7), (8) that

$$\begin{aligned} &\tilde{I}_i^b = I_i^b(\tilde{V}_m^b, c_{i,L}^b, c_{i,R}^b), \quad i = 2, 3, \\ &\tilde{I}_k^{pump} = I_k^{pump}(\tilde{V}_m^b, c_{1,L}^b, c_{1,R}^b, c_{2,L}^b, c_{2,R}^b), \quad k = 1, 2. \end{aligned} \tag{48}$$

Note that we have replaced ∂_t by $\frac{d}{dt}$ to reflect the fact that spatial variation is removed at the leading order. Similarly,

$$C_m \frac{d}{dt}\tilde{V}_m^a = -\left(\tilde{I}_1^{VG} + \tilde{I}_1^R + \tilde{I}_2^{VG} + \tilde{I}_2^R + \tilde{I}_2^{Kir} + \tilde{I}_3^{VG}\right), \tag{49}$$

where the above $\tilde{I}_i$ $(i = 1, 2, 3)$ are defined by replacing V_m^a and $c_{i,\pm}^a$ on the right-hand side of (3), (4), (6) by the bulk quantities $\tilde{V}_m^a, c_{i,R}^a$ and $c_{i,L}^a$. Eqs. (47) and (49) constitute the membrane model (ODE model) for computing the two membrane potentials. Eq. (49) with the specific formulas of currents in Section 5.1 is exactly the same as in Xu and Lavan (2008), which generates APs. Eq. (47) is not explicitly given in Xu and Lavan (2008).

Next we briefly show that $\tilde{V}_m^b$ (or approximately V_m^b) does not vary during the dynamic process, which is believed to be true in other works (Gotter et al., 1998; Xu and Lavan, 2008). Let $\tilde{V}^*$ be the local equilibrium of $\tilde{V}_m^b$ at resting state, then $\tilde{V}_m^b = \tilde{V}^*$ is a stable equilibrium in general. Locally (47) can be written as

$$C_m \frac{d}{dt}\tilde{V}_m^b = -C_b(\tilde{V}_m^b - \tilde{V}^*), \quad C_b > 0, \tag{50}$$

where $C_m \approx 4.5 \times 10^{-8}$. With specific formulas in Section 5.1, Fig. 2 shows $f(\tilde{V}_m^b)$ in (47) in a proper range for membrane potential $\tilde{V}_m^b$. It can be seen that there is a stable equilibrium near -3.2 (or -83 mV before scale), and we have $C_b \approx 0.01$. From Section 4.1, we showed that ψ is a constant respectively in the bulk of (a, b) or $(b, 1)$. The constant $\psi_R^a = \psi_L^b$ in (a, b) is controlled by the dynamics of innervated membrane, and hence this causes some perturbation in $\tilde{V}_m^b = \psi_L^b - \psi_R^b$. Since $\tilde{V}^*$ is a stable equilibrium, $\tilde{V}_m^b$ always recovers to $\tilde{V}^*$ after perturbation. This is done by adjusting the constant $\psi_R^b = \psi(1)$ in the bulk of $(b, 1)$, since there is no restriction for $\psi(1)$.

In summary, we have shown that ψ is a constant in each bulk of the three regions, and the three constants are determined by the two membrane potentials. Using the boundary condition at $x = 0$, ψ remains as 0 in the region $x < a$. During an AP at $x = a$, $\tilde{V}_m^a$ increases and ψ will increase in the region $a < x < b$. Since the non-innervated membrane is at equilibrium all the time, i.e., $\tilde{V}_m^b$ is fixed, ψ in the region $x > b$ has to increase accordingly. This explains why there is a high transcellular potential.

5. Numerical analysis

In this section, we adopt specific formulas for the membrane currents in the model, and then show the numerical results by solving the dimensionless PNP system in Section 3.

5.1. Formulas of currents

In this subsection, we present the formulas of currents in (3), (4), (6)–(8). The original parameter values in the following formulas are given in Appendix B, while the dimensionless formulas and parameter values are given in Appendix C.

The currents through voltage-gated channels in (3) are given by the classical HH model (Malmivuo and Plonsey, 1995; Hodgkin and Huxley, 1990)

$$I_i^{VG} = G_i(V_m^a - V_i^a) = G_i\left(\psi_+^a - \psi_-^a - \frac{k_B T}{z_i e_0}\ln\frac{c_{i,-}^a}{c_{i,+}^a}\right), \quad i = 1, 2, 3, \tag{51}$$

where the Nernst potential V_i^a is defined as the last term in the bracket. The conductances G_i are given by Xu and Lavan (2008)

$$G_1 \equiv \bar{g}_{Na} m^3\, h + \bar{g}_{Na,leak}, \quad G_2 \equiv \bar{g}_K n^4 + \bar{g}_{K,leak}, \quad G_3 \equiv \bar{g}_{Cl}, \tag{52}$$

where $\bar{g}_{Na}, \bar{g}_K, \bar{g}_{Cl}, \bar{g}_{Na,leak}, \bar{g}_{K,leak}$ are constants, and m, h, n are the gating variables whose dynamics are given in Appendix A. Following Xu and Lavan (2008), we assume that there is no chloride channel on innervated membrane and set $\bar{g}_{Cl} = 0$.

The current from the Kir channel in (4) is given by

$$I_2^{Kir} = \frac{\bar{g}_{Kir}(V_m^a - V_2^a)}{1 + e^{\frac{n_1 F}{RT}(V_m^a - V_2^a + n_2)}}, \tag{53}$$

where $\bar{g}_{Kir}$ is the maximum conductance of Kir channel, $F = e_0 N_A$ is Faraday's constant, $R = k_B N_A$ is the gas constant, and n_1 and n_2 are two parameters.

In Xu and Lavan (2008), the currents through the receptor in (6) are restricted to the case

$$I_1^R = I_1^*, \quad I_2^R = 0, \tag{54}$$

where I_1^* is given by Sheridan and Lester (1977); Magleby and Stevens (1972); Xu and Lavan (2008)

$$I_1^* = \frac{[A]^2 \bar{g}_R e^{-\alpha t}}{[A]^2 + 2[A]\frac{k_{-2}}{k_{+2}} + \frac{k_{-1}k_{-2}}{k_{+1}k_{+2}}}(V_m^a - V_0), \quad 2k_{-2} = \alpha = \alpha_0 e^{\frac{V_m^a}{V_1}}, \tag{55}$$

where $\bar{g}_R$ is the conductance for the open receptors, and α_0, V_0, V_1 are parameters determined from experimental data.

At the non-innervated membrane $x = b$, Goldman-Hodgkin-Katz (GHK) model (Hille et al., 2001; Xu and Lavan, 2008) is used for the currents in (7)

$$I_i^b = P_i z_i^2 \frac{V_m^b F^2\left(c_{i,-}^b - c_{i,+}^b e^{-\frac{z_i F}{RT}V_m^b}\right)}{RT\left(1 - e^{-\frac{z_i F}{RT}V_m^b}\right)}, \quad i = 2, 3, \tag{56}$$

where P_i is the permeability. Other choices could be the HH type currents as in (51) with fixed conductances.

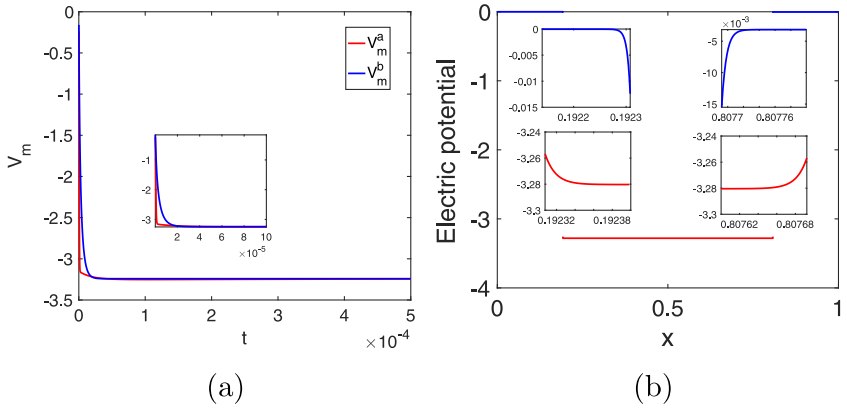

Fig. 3. Numerical results to generate the resting state in step (I); (a) the dynamics of membrane potential V_m (b) Distribution of electric potential at resting state.

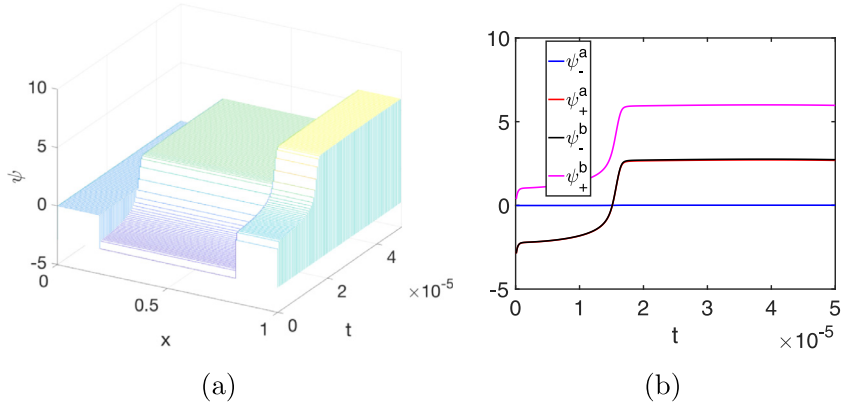

Fig. 4. The variation and dynamics of electric potential, (a) position and time dependence, and (b) dynamics at four spatial locations, i.e., both sides of the two membranes.

The pumps (Goldshlegger et al., 1987; Novotny and Jakobsson, 1996) in both membranes are not needed since it has little impact on fast AP dynamics. It restores the equilibrium Na^+ and K^+ concentrations over a much longer timeframe. Thus we set in (8) that

$$I_i^{pump} = 0, \quad i = 1, 2, 3. \tag{57}$$

5.2. Numerical results

The computation is carried out in two steps: (I) the resting state is generated when the receptor is closed; and (II) the dynamics of the electric potential is simulated when the receptor is activated.

In step (I), the resting state is generated by setting $I_1^R = I_2^R = 0$ in (6). Fig. 3(a) shows the dynamics of membrane potentials V_m^a and V_m^b. At the innervated membrane $x = a$, the flux of potassium ion is negative, i.e. from IC region to EC region, while the flux of sodium ion is positive. At the non-innervated membrane $x = b$, fluxes of potassium and chloride ions are from IC region to EC region. After certain time period, the net current across each membrane tends to 0. The resting potentials are calculated as

$$\begin{aligned} V_m^a|_{t=5\times10^{-4}} &= \psi_+^a - \psi_-^a = -3.2443, \\ V_m^b|_{t=5\times10^{-4}} &= \psi_-^b - \psi_+^b = -3.2414, \end{aligned} \tag{58}$$

and the original values before scaling is about -84 mV (similar to the value in Xu and Lavan (2008)). Fig. 3(b) shows the distributions of electric potential ψ at the resting state. It indicates that the electric potential ψ is almost a constant at each of the three bulk regions, and there are thin BLs on both sides of the membranes. The variation of ψ in the BLs is consistent with the estimates in (45).

In step (II), the ACh receptors are activated, inducing extra flux of sodium ion, given by (54), (55). The resting state in Fig. 3(b) is used as the initial state. Fig. 4 shows the dynamics of electric potential up to full depolarization. Fig. 4(a) is the position and time dependence of ψ, and Fig. 4(b) shows dynamics at four spatial locations, i.e., both sides of the two membranes at $x = a$ and b. Fig. 4(b) shows that the electric potential on the left side of the innervated membrane is almost a constant 0, determined by the left boundary condition. The electric potentials on the right-side of the innervated membrane and on the left-side of the non-innervated membrane are almost identical, indicating that ψ is almost a constant in the bulk of the IC region.

Fig. 4 (a) can be further illustrated by snapshots at various times as depicted in Fig. 5. Note that, unlike the subfigures in Fig. 3(b), BLs are hardly observable in the scale of Fig. 5. From Figs. 3(b) to 5(a), electric potential ψ in the IC space increases rapidly since receptors are open and more sodium ions flow through the innervated membrane from the EC space into the IC space. From Fig. 5(a) to (b), electric potentials adjust slightly, due to the synergy of various fluxes and conductances. This corresponds to small variations by the curves for $t \in [0.2, 1.2] \times 10^{-5}$ in Fig. 4(b). The electric potentials in (a, b) and $(b, 1)$ increase significantly again from From Fig. 5(b) to (d). Finally, the membrane potential at the innervated membrane reaches up to 2.7 (70 mV in physical units) and transcellular potential reaches about 6.0 (155 mV), while the membrane potential at the non-innervated membrane remains at its resting equilibrium all the time. Figs. 4 and 5 confirm our asymptotic analysis that ψ remains as piecewise constants in the bulk regions, and the estimated time scale in (22) is also confirmed. This property of constant electric potential in the bulk of IC region provides the justification that the

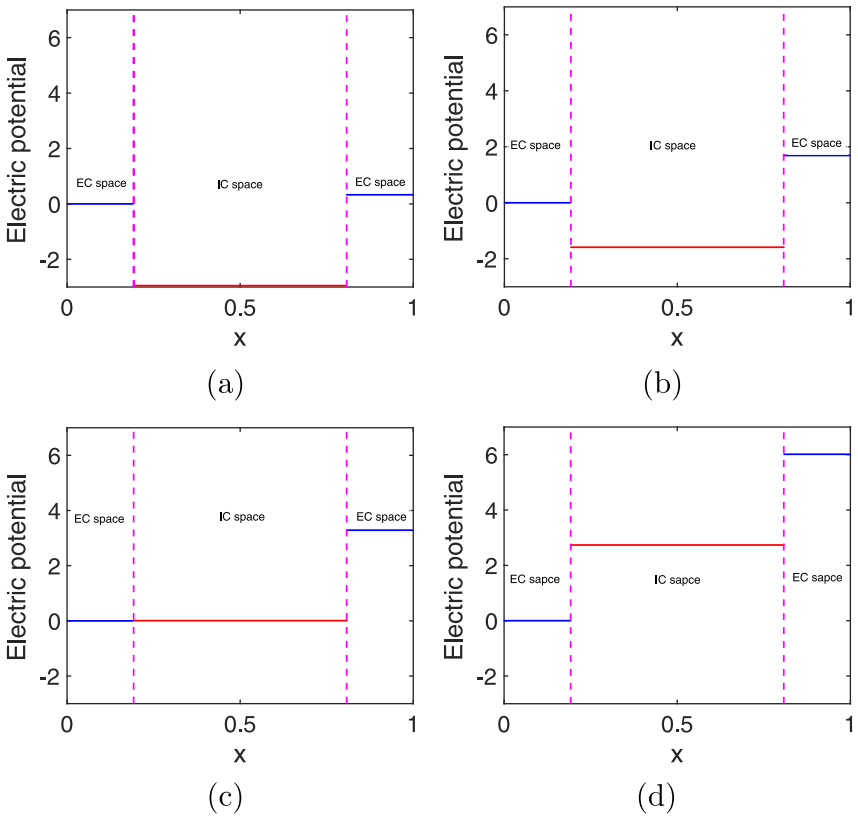

Fig. 5. The electric potential at (a) $t = 10^{-6}$, (b) $t = 1.2 \times 10^{-5}$, (c) $t = 1.55 \times 10^{-5}$, (d) $t = 4.0 \times 10^{-5}$, where EC and IC spaces stand for extracellular and intracellular spaces, respectively.

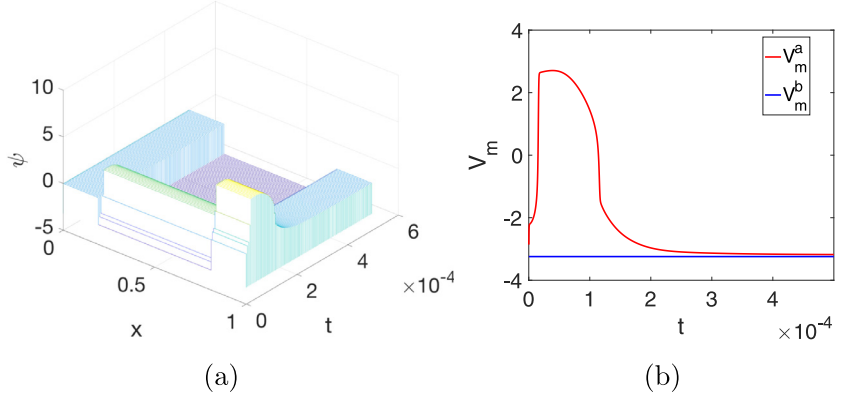

Fig. 6. The variation and dynamics of electric potential for relatively long time, (a) the position and time dependence, and (b) the dynamics of two membrane potentials.

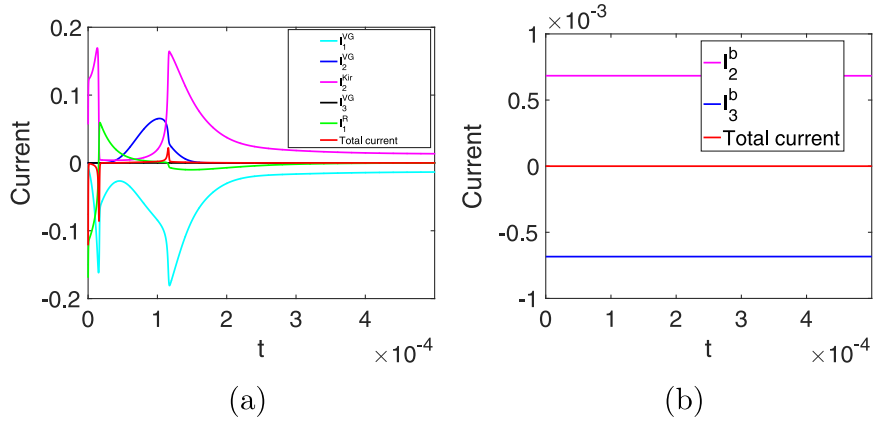

Fig. 7. The dynamics of all nonzero membrane currents in (17) and the total current: (a) at the innervated membrane $x = a$, (b) at the non-innervated membranes $x = b$.

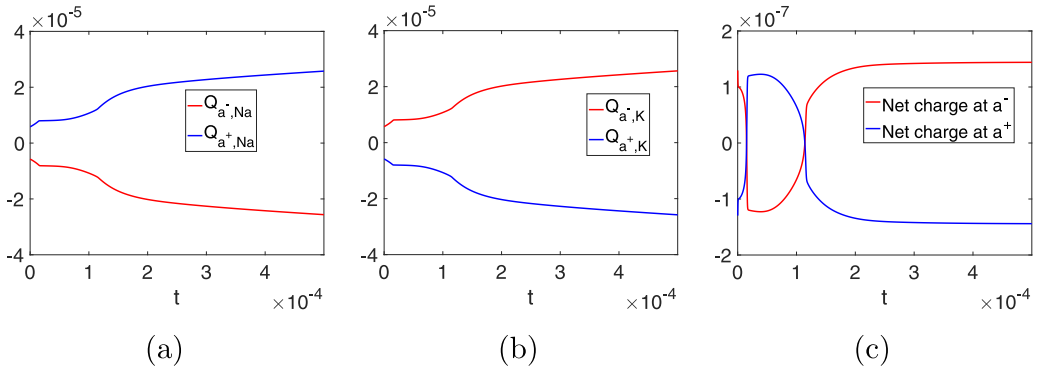

Fig. 8. Time history of excessive charges at both sides of innervated membrane: (a) for Na^+, (b) for K^+, (c) the net excessive charge.

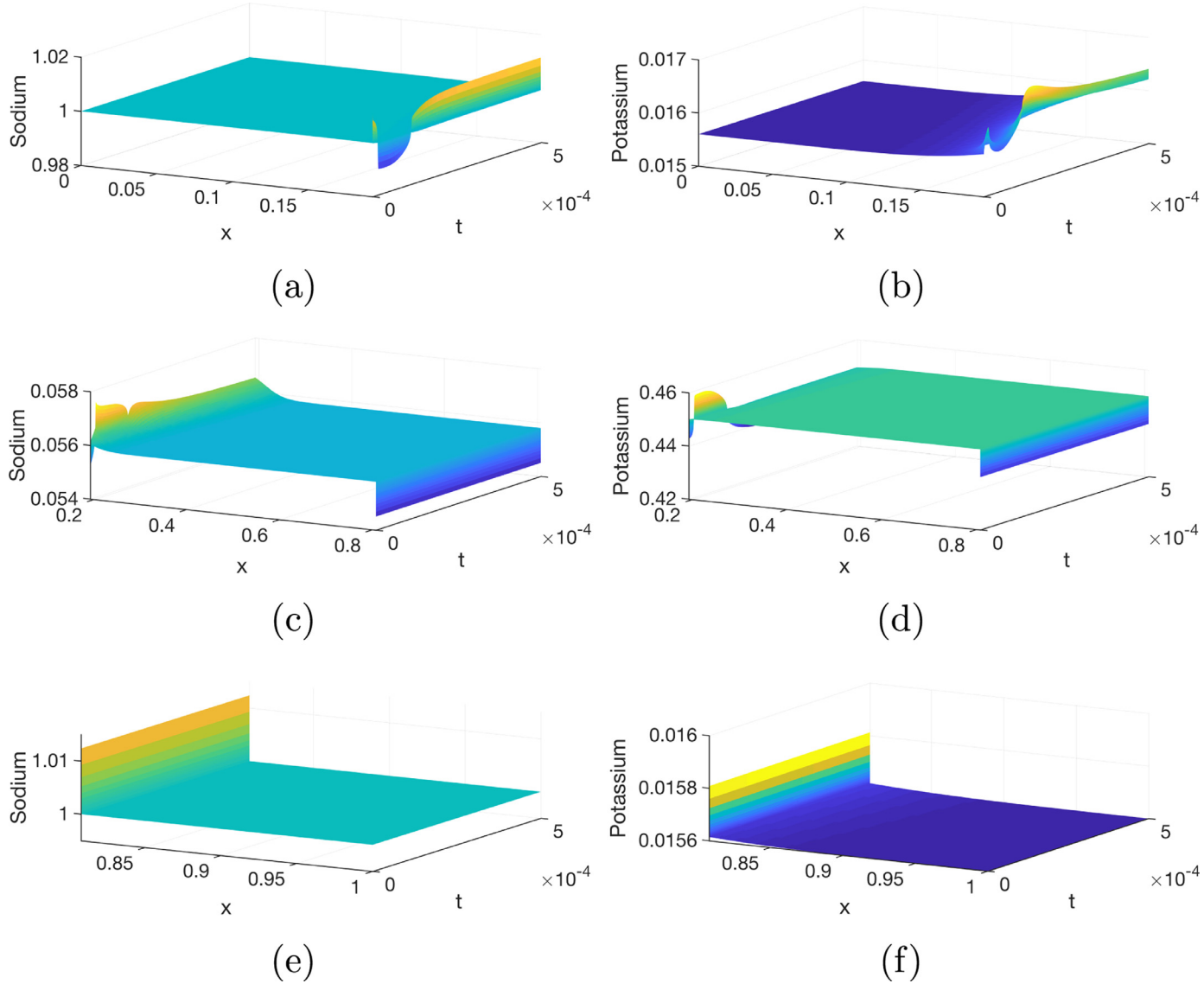

Fig. 9. The dynamics and variation of concentrations: sodium ion in (a) the left extracellular space, (c) intracellular space, and (e) right extracellular space; and potassium ion in (b) left extracellular space (d) intracellular space and (f) right extracellular space.

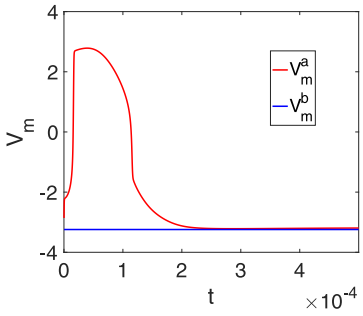

Fig. 10. The two membrane potentials with the receptor open for both sodium and potassium ions.

transcellular potential, $\psi(1)-\psi(0)$, can be obtained by the superposition of the two membrane potentials, $V_m^a - V_m^b$.

Fig. 6 shows the dynamics for the entire course of the AP. Fig. 6(a) shows the dependence of the electric potential in both space and time, and Fig. 6(b) shows the membrane potentials at $x = a$ and b. The previous Fig. 4 corresponds to the rising phase of Fig. 6. It is clear that the membrane potential V_m^a at the innervated membrane $x = a$ experiences an AP (Gotter et al., 1998; Xu and Lavan, 2008). It starts from resting state −83.8 mV, peaks at about 70 mV, and finally recovers to the resting state. The membrane potential V_m^b at $x = b$ keeps at its resting state all the time. These are consistent with our asymptotic analysis.

To examine the roles played by each individual flux, we plot the all the nonzero fluxes (currents) and total current at the innervated and non-innervated membranes in Fig. 7(a) and (b). The red line in Fig. 7(a) denotes the total current at the innervated membrane, which remains small. Initially, an extra current is induced by flux of sodium ion through the receptor, when acetylcholine (ACh) is released near the receptors. As a result, voltage-gated Na^+ channels are activated, and I_1^{VG} increases during the depolarization phase of the AP. In the meantime, since V_m^a changes rapidly, the flux in the opposite direction from Kir channels becomes significant and balances most fluxes from receptor and Na^+ channels. Near the peak of the AP, fluxes from Kir channel, Na^+ channels and receptor become much smaller and the current from receptor is reversed. During the repolarization phase of AP, voltage-gated K^+ channels open and play a significant role to balance other fluxes. Subsequently, fluxes from Na^+ and Kir channels increase again and balance each other. Finally, all fluxes decay to 0 or negligible values when it restores back to the resting state. In Fig. 7(b), fluxes at the non-innervated membrane are steady and small, since there are no receptors there. This leads to a constant membrane potential V_m^b as shown in Fig. 6(b).

In our analysis, we interpreted the innervated and non-innervated membranes as capacitors. Now we verify this approximation and compute excessive charge at each side of the membranes. As in (41), we define excessive charge for each ion species at two sides of the innervated membrane as

$$Q_{a^-,i} = \int_0^a c_i(x) - c_i(0)dx, \quad Q_{a^+,i} = \int_a^{0.5} c_i(x) - c_i(0.5)dx, \quad i = 1, 2, 3. \tag{59}$$

The total excessive charges, namely the net charges, at the left and right sides of the innervated membrane are computed by $\sum_{i=1}^3 z_i Q_{a^-,i}$ and $\sum_{i=1}^3 z_i Q_{a^+,i}$. Similar quantities can be computed at the non-innervated membrane. Fig. 8(a) and (b) present the time history of excessive charges of K^+ and Na^+ at both sides of innervated membrane during an AP. Fig. 8(c) shows the net charge at both sides of the innervated membrane, which indicates that the net charge is much smaller than excessive charges of Na^+ and K^+. These two net charges have the same magnitude but

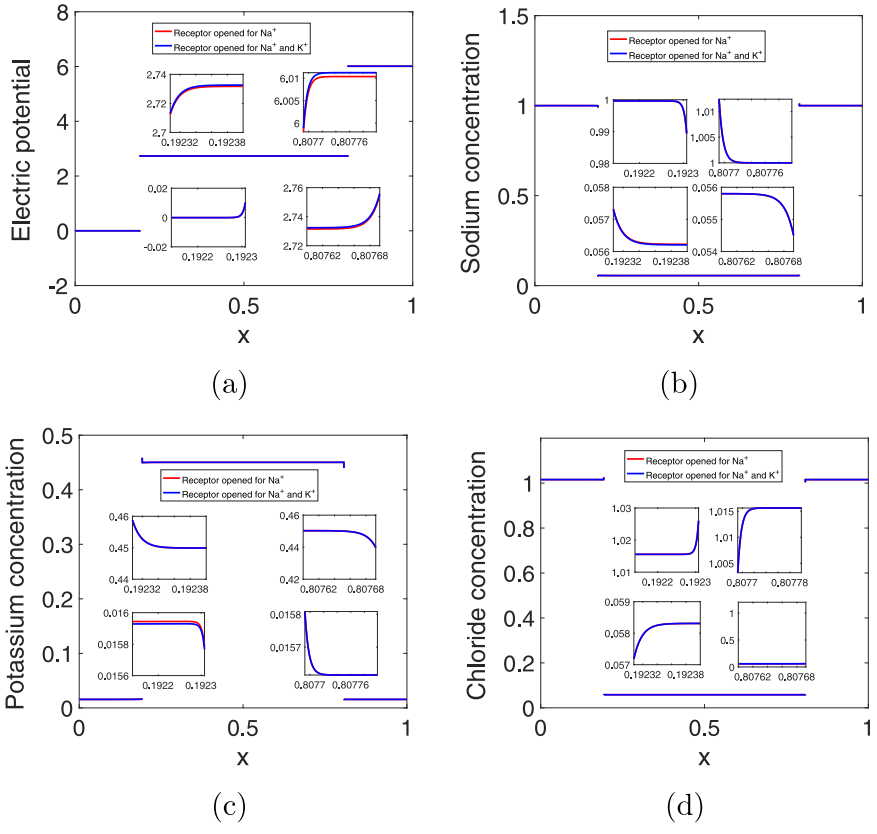

Fig. 11. The comparison of electric potential and the concentrations Na^+, K^+ and Cl^- at $t = 5 \times 10^{-5}$ for the two cases, with or without potassium flux through the receptor.

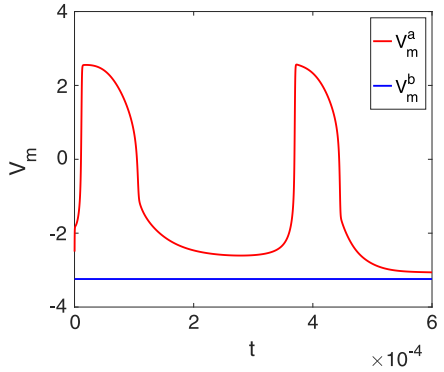

Fig. 12. The dynamics of two membrane potentials with $\bar{g}_R = 800\text{C}/(\text{V}\cdot\text{s}\cdot\text{m}^2)$, $V_1 = 86$ mV and $\alpha_0 = 1.23$ ms^{-1}.

opposite signs, which implies that the membrane does act as a capacitor during AP. The profiles are similar to that of V_m^a in Fig. 6(b), as they can be approximated by $\pm C_m V_m^a$ (like equations (42), (43)). This agrees with our analysis and the results using the membrane model (Xu and Lavan, 2008).

Fig. 9 shows the dynamics and variation of concentrations of sodium and potassium ions in three regions (Chloride ion is omitted for brevity). In the bulk, it is clear that the concentrations remain almost constants and vary only near the two membranes. The variation near the membrane is also at a small scale, which justifies the use of bulk value as leading approximation in the previous analysis. It further implies that AP is indeed caused by a small amount of ions' movement across the membrane, compared with a much larger quantity in the bulk regions. Near the innervated membrane $x = a$, ion concentrations adjust during AP, while at the non-innervated membrane $x = b$ ion concentrations do not vary, which is consistent with its membrane potential V_m^b being steady at resting state.

So far, we have considered the case that only sodium ions go through ACh receptors, but in general ACh receptors are not selective and allow currents of many cations (Adams, 1981). In the following, we consider the case that the receptors are open for both Na^+ and K^+. We set

$$I_1^R = 2I_1^*, \quad I_2^R = -I_1^*, \tag{60}$$

so that the total current across the receptors is still I_1^*, given by (55). Fig. 10 presents the profiles of two membrane potentials in this case, which are almost identical to Fig. 6(b). At $t = 5\times10^{-5}$, Fig. 11 compares the two cases for the spatial variation of the electric potential and the three ion concentrations Na^+, K^+ and Cl^-. In each subfigure, the blue and red lines represent the cases with and without potassium flux through the receptors. Fig. 11(a) shows that the difference of electric potentials is also negligible (about 9×10^{-4}) for both cases. Since the receptors are on the innervated membrane, there is a small difference (similar scale 10^{-4}) in concentrations near the innervated membrane. Therefore, the interpretation of currents from receptors has little impact on the spatial variation and dynamical process.

Before we end this section, we would like to discuss a common issue in modeling a complex system with parameter uncertainties. Most parameters in Appendix B are either constants or determined by experiments and considered to be reliable. However, this is not the case for some parameters such as $\bar{g}_R$, which is reported to be in the range $[700, 2000]\text{C}/(\text{V}\cdot\text{s}\cdot\text{m}^2)$. The lower bound 700 is used in our computations. In addition, the values of parameters V_1 and α_0 could vary with different temperatures. To investigate the effect of these parameters, we performed computations by using the following values $\bar{g}_R = 800\text{C}/(\text{V}\cdot\text{s}\cdot\text{m}^2)$, $V_1 = 86$ mV and $\alpha_0 = 1.23$ ms^{-1} (Sheridan and Lester, 1977). Fig. 12 shows the dynamics of the membrane potentials. It can be seen that there is repeated AP on the left innervated membrane, instead of just one AP in the previous computation. We speculate that this could be the case when electrocytes operate under different temperatures. But a more careful investigation is needed before we can reach any concrete conclusions. Mathematically, these parameters affect the current strength through ACh receptors in (6), which increases with a larger $\bar{g}_R$ and decays more slowly with a smaller α. When this receptor initiated current is sufficiently strong when the membrane repolarizes after generating its first AP, a new AP could be triggered.

6. Conclusions

In this paper, we have formulated a mathematical model to study the mechanism of electric potential generation in electric eels. Our PNP model explores AP generation at the innervated membrane through the activation of the ACh receptors and Na^+ and K^+ channels, and shows that electric potential holds almost uniform across the entire EC and IC bulk regions. In addition, we show that the dynamics of membrane potentials can be approximated by interpreting membranes as capacitors, and the non-innervated membrane is kept at resting equilibrium state all the time. Our asymptotic analysis justifies the superposition of innervated and non-innervated membrane potentials to constitute the transcellular potential observed in the previous membrane model (Xu and Lavan, 2008) and our numerical solution of the PNP system confirms that. Finally, we note that we have considered the issue of electric potential generation of electrocyte in an open circuit. In this case, we have showed that there is almost no current in the EC and IC spaces, and the transcellular potential is generated by two membranes acting as capacitors. During discharge in a closed circuit, there will be an external current and other interesting interactions but the same framework should be applicable. The project for the case of a closed circuit is ongoing, and we plan to investigate the combined effect of electric generation and discharge.

Acknowledgments

This work is supported in part by the Natural Science and Engineering Research Council (NSERC) of Canada and the Fields Institute.

Appendix A. The dynamic system of *m*, *n*, *h*

The dynamic system of m, n, h is

$$\begin{aligned}\frac{dn}{dt} &= \alpha_n(1-n) - \beta_n n,\\ \frac{dm}{dt} &= \alpha_m(1-m) - \beta_m m,\\ \frac{dh}{dt} &= \alpha_h(1-h) - \beta_h h.\end{aligned} \tag{A.1}$$

The coefficients depend on V_m^a and are given by

$$\begin{aligned}\alpha_n &= 2.38\times10^3\cdot e^{\frac{V_m^a+0.0164}{0.0472}}, \quad \beta_n = 1.71\times10^3\cdot e^{-\frac{V_m^a+0.0164}{0.0184}}\\ \alpha_m &= 2.64\times10^4\cdot e^{\frac{V_m^a+0.0618}{0.0295}}, \quad \beta_m = 2.59\times10^4\cdot e^{-\frac{V_m^a+0.0618}{0.0242}}\\ \alpha_h &= 1.08\times10^3\cdot e^{-\frac{V_m^a+0.0545}{0.00784}}, \quad \beta_h = 1.49\times10^3/(0.0745+e^{-\frac{V_m^a+0.0545}{0.0129}}),\end{aligned} \tag{A.2}$$

where α_i and β_i $(i = n, m, h)$ are dimensionless parameters scaled by $1/(16.9\,\text{s})$ (where 16.9 s comes from the diffusion time scale in this paper), V_m^a are values in unit Volt. With $V_m^a = -0.084$ V, we obtain the steady state solution

$$n_0 = 0.008458, \quad m_0 = 0.1622, \quad h_0 = 0.9967, \tag{A.3}$$

which are used as initial values of the time-dependent problem to simulate action potential.

Appendix B. The parameters and data

The data are mainly from Hodgkin and Huxley (1990); Pods et al. (2013); Sheridan and Lester (1977); Magleby and Stevens (1972) and the book in Liu and Eisenberg (2014). The temperature in Xu and Lavan (2008) is set to be 27°C so we get $T = 300.15$ K. The other constants are

$$k_B = 1.38 \times 10^{-23}\text{J/K} \quad N_A = 6.022 \times 10^{23}/\text{mol},$$
$$e_0 = 1.602 \times 10^{-19}\text{C} \quad \epsilon_0 = 8.854 \times 10^{-12}\text{C}/(\text{V}\cdot\text{m}),$$
$$F = e_0 N_A \quad R = k_B N_A.$$

The typical bulk concentrations (see Gotter et al. (1998)) for Na^+, K^+, Cl^- are

	c_1, Na^+	c_2, K^+	c_3, Cl^-	q
Extracellular	160 mM	2.5 mM	162.5 mM	0
Intracellular	8.928 mM	72.048 mM	9.328 mM	−71.648 mM

which are used as initial conditions (scaled by c_0 below). Some typical values are

$$\epsilon_r = 80, \quad \epsilon_r^m = 2, \quad c_0 = 160\,\text{mM} = 160\,\text{mol/m}^3,$$
$$h_m = 5\,\text{nm}, \quad L = 130\ \mu\text{m}, \quad a = 25\ \mu\text{m}, \quad b = 105\ \mu\text{m}, \tag{B.1}$$
$$D_0 = 10^{-9}\,\text{m}^2/\text{s}, \quad D_1 = 1.33D_0, \quad D_2 = 1.96D_0, \quad D_3 = 2.03D_0.$$

The conductances and parameters in flux formulas are given by Xu and Lavan (2008); Magleby and Stevens (1972)

$$\bar{g}_{Na} = 157\,\text{mS/cm}^2 = 1570\,\text{C}/(\text{V}\cdot\text{s}\cdot\text{m}^2),$$
$$\bar{g}_K = 320\,\text{C}/(\text{V}\cdot\text{s}\cdot\text{m}^2), \quad \bar{g}_{Cl} = 0\,\text{C}/(\text{V}\cdot\text{s}\cdot\text{m}^2),$$
$$\bar{g}_{Na,leak} = 0.2761\,\text{C}/(\text{V}\cdot\text{s}\cdot\text{m}^2) \quad \bar{g}_{K,leak} = 31.5390\,\text{C}/(\text{V}\cdot\text{s}\cdot\text{m}^2),$$
$$\bar{g}_{Kir} = 591\,\text{C}/(\text{V}\cdot\text{s}\cdot\text{m}^2), \quad \bar{g}_R = 700\,\text{C}/(\text{V}\cdot\text{s}\cdot\text{m}^2),$$
$$P_1 = 0, \quad P_2 = 1.12 \times 10^{-6}\text{m/s}, \quad P_3 = 7.63 \times 10^{-8}\text{m/s}, \tag{B.2}$$
$$n_1 = 1.45, \quad n_2 = -0.0630\,\text{V}, \quad [A] = 0.1\text{mol/m}^3,$$
$$V_0 = 0, \quad V_1 = 125.79\ \text{mV}, \quad \alpha_0 = 1.67\ \text{ms}^{-1} = 1.67 \times 10^3\ \text{s}^{-1},$$
$$k_{+2} = 7 \times 10^3\ \text{m}^3/(\text{mol}\cdot\text{s}), \quad k_{-1}/k_{+1} = 2 \times 10^{-2}\ \text{mol/m}^3.$$

From the above data, we get the scales

$$\frac{k_B T}{e_0} \approx 25.9\,\text{mV}, \quad \frac{L^2}{D_0} = 16.9\,\text{s}, \quad \lambda_D = 1.0893 \times 10^{-9}\ \text{m},$$
$$G_0 = 4592.2\,\text{C}/(\text{V}\cdot\text{s}\cdot\text{m}^2), \quad P_0 = 7.69 \times 10^{-6}\ \text{m/s}, \tag{B.3}$$
$$I_0 = 118.74\ \text{C}/(\text{s}\cdot\text{m}^2).$$

Appendix C. The dimensionless parameters and formulas

The dimensionless parameters are

$$\epsilon = 8.38 \times 10^{-6}, \quad \epsilon_m = 1.32 \times 10^{-6},$$
$$h_m = 3.85 \times 10^{-5}, \quad a = 0.1923, \quad b = 0.8077,$$
$$D_1 = 1.33, \quad D_2 = 1.96, \quad D_3 = 2.03, \quad q = -0.4478,$$
$$\alpha_0 = 2.82 \times 10^4, \quad n_1 = 1.45, \quad n_2 = -2.4366,$$
$$\bar{g}_{Na} = 0.3419, \quad \bar{g}_K = 0.06968, \quad \bar{g}_{Cl} = 2.18 \times 10^{-4}, \tag{C.1}$$
$$\bar{g}_{Na,leak} = 6.0123 \times 10^{-5} \quad \bar{g}_{K,leak} = 6.8679 \times 10^{-3},$$
$$\bar{g}_{Kir} = 0.1287, \quad \bar{g}_R = 0.1524, \quad V_0 = 0, \quad V_1 = 4.86,$$
$$[A] = 6.25 \times 10^{-4}, \quad k_{+2} = 1.89 \times 10^7, \quad k_{-1}/k_{+1} = 1.25 \times 10^{-4},$$
$$P_1 = 0, \quad P_2 = 0.1455, \quad P_3 = 0.009914.$$

The dimensionless formulas of currents are

$$I_i^{VG} = G_i\left(V_m^a - \frac{1}{z_i}\ln\frac{c_{i,-}^a}{c_{i,+}^a}\right),$$
$$I_2^{Kir} = \frac{\bar{g}_{Kir}(V_m^a - V_2^a)}{1 + e^{n_1(V_m^a - V_2^a + n_2)}}, \quad V_m^a = \psi_+^a - \psi_-^a, \quad V_2^a = \frac{1}{z_2}\ln\frac{c_{2,-}^a}{c_{2,+}^a},$$

$$I_i^b = P_i z_i^2 \frac{V_m^b\left(c_{i,-}^b - c_{i,+}^b e^{-z_i V_m^b}\right)}{(1 - e^{-z_i V_m^b})}, \tag{C.2}$$

and the form of I_1^* in (55) will not change.

The functions F_{iR} and F_{iL} in (31) are given by

$$F_{jR} = \sqrt{\frac{c_{jR}}{c_{3R}}}\sqrt{2c_{jR}}\left(e^{(\psi_R - \psi_+^b)/2} - 1\right), \quad j = 1, 2,$$
$$F_{3R} = \sqrt{2c_{3R}}\left(e^{(\psi_+^b - \psi_R)/2} - 1\right),$$
$$F_{jL} = \sqrt{\frac{c_{jL}}{c_{3L}}}\sqrt{2c_{jL}}\left(e^{(\psi_L - \psi_-^b)/2} - 1\right), \quad j = 1, 2,$$
$$F_{3L} = \sqrt{2c_{3L}}\left(e^{(\psi_-^b - \psi_L)/2} - 1\right), \tag{C.3}$$

where subscript L and R mean the left and right limits from the bulk solutions.

Appendix D. Estimates of (45) and (46)

As the BL is $O(\lambda_D)$, by mean value theorem, we have

$$|\psi(b^+) - \psi(1)| \sim O(\lambda_D|\partial_x\psi|(\xi, t)) \sim O(\lambda_D \frac{\epsilon_m^2}{\epsilon^2}\frac{|V_m^b|}{h_m}), \quad \xi \in (b, 1), \tag{D.1}$$

in other words, we get

$$\frac{|\psi(b^+) - \psi(1)|}{|V_m^b|} \sim O(\frac{\epsilon_m^2}{\epsilon^2}\frac{\lambda_D}{h_m}), \tag{D.2}$$

In the case of $c_b = 160$ mM, $h_m = 5$ nm and $\lambda_D = 1$ nm, we obtain

$$\frac{|\psi(b^+) - \psi(1)|}{|V_m^b|} \sim O(\frac{1}{200}). \tag{D.3}$$

Similarly we get

$$\frac{|\psi(b^-) - \psi(0.5)|}{|V_m^b|} \sim O(\frac{1}{200}). \tag{D.4}$$

Combining the two, we get

$$\frac{|\psi(1) - \psi(0.5)|}{|V_m^b|} \sim O(\frac{101}{100}), \tag{D.5}$$

and hence it is approximately well if we replace V_m^b by bulk difference $\psi(1) - \psi(0.5)$ (this is also $\tilde{V}_m^b$ as ψ is constant in bulk). Similar arguments apply to V_m^a.

References

Adams, P., 1981. Acetylcholine receptor kinetics. J. Membr. Biol. 58 (3), 161–174.
Altamirano, M., 1955. Electrical properties of the innervated membrane of the electroplax of electric eel. J. Cell. Comp. Physiol. 46 (2), 249–277.
Bezanilla, F., 2007. Voltage-gated Ion Channels. In: Biological Membrane Ion Channels. Springer, pp. 81–118.
Brown, M., 1950. The electric discharge of the electric eel. Electr. Eng. 69 (2), 145–147.
Catania, K.C., 2015a. Electric eels concentrate their electric field to induce involuntary fatigue in struggling prey. Current Biol. 25 (22), 2889–2898.
Catania, K.C., 2015b. Electric eels use high-voltage to track fast-moving prey. Nat. Commun. 6, 8638.
Catania, K.C., 2017a. Electrical potential of leaping eels. Brain Behav. Evol. 89 (4), 262–273.
Catania, K.C., 2017b. Power transfer to a human during an electric eel's shocking leap. Current Biol. 27 (18), 2887–2891.
Chakrapani, S., Bailey, T.D., Auerbach, A., 2004. Gating dynamics of the acetylcholine receptor extracellular domain. J. Gen. Physiol. 123 (4), 341–356.
Coates, C., 1950. Electric fishes. Electr. Eng. 69 (1), 47–51.
Dunlap, K.D., McAnelly, M.L., Zakon, H.H., 1997. Estrogen modifies an electrocommunication signal by altering the electrocyte sodium current in an electric fish, sternopygus. J. Neurosci. 17 (8), 2869–2875.
Gardner, C.L., Jones, J.R., 2011. Electrodiffusion model simulation of the potassium channel. J. Theor. Biol. 291, 10–13.

George, S., Foster, J.M., Richardson, G., 2015. Modelling in vivo action potential propagation along a giant axon. J. Math. Biol. 70 (1–2), 237–263.
Goldshlegger, R., Karlish, S., Rephaeli, A., Stein, W.D., 1987. The effect of membrane potential on the mammalian sodium-potassium pump reconstituted into phospholipid vesicles.. J. Physiol. (Lond.) 387 (1), 331–355.
Gotter, A.L., Kaetzel, M.A., Dedman, J.R., 1998. Electrophorus electricus as a model system for the study of membrane excitability. Comp. Biochem. Physiol. Part A 119 (1), 225–241.
Hille, B., et al., 2001. Ion Channels of Excitable Membranes, 507. Sinauer Sunderland, MA.
Hodgkin, A., Huxley, A., 1990. A quantitative description of membrane current and its application to conduction and excitation in nerve. Bull. Math. Biol. 52 (1–2), 25–71.
Hodgkin, A.L., Huxley, A.F., 1952. A quantitative description of membrane current and its application to conduction and excitation in nerve. J. Physiol. (Lond.) 117 (4), 500–544.
Humayun, M.S., Weiland, J.D., Fujii, G.Y., Greenberg, R., Williamson, R., Little, J., Mech, B., Cimmarusti, V., Van Boemel, G., Dagnelie, G., et al., 2003. Visual perception in a blind subject with a chronic microelectronic retinal prosthesis. Vis. Res. 43 (24), 2573–2581.
Kenny, A., Plank, M.J., David, T., 2018. Macro scale modelling of cortical spreading depression and the role of astrocytic gap junctions. J. Theor. Biol. 458, 78–91.
Keynes, R., Martins-Ferreira, H., 1953. Membrane potentials in the electroplates of the electric eel. J. Physiol. (Lond.) 119 (2–3), 315–351.
Kilic, M.S., Bazant, M.Z., Ajdari, A., 2007a. Steric effects in the dynamics of electrolytes at large applied voltages. i. double-layer charging. Phys. Rev. E 75 (2), 021502.
Kilic, M.S., Bazant, M.Z., Ajdari, A., 2007b. Steric effects in the dynamics of electrolytes at large applied voltages. ii. modified poisson-nernst-planck equations. Phys. Rev. E 75 (2), 021503.
Lissmann, H., 1958. On the function and evolution of electric organs in fish. J. Exp. Biol. 35 (1), 156–191.
Liu, J.-L., Eisenberg, B., 2014. Poisson-nernst-planck-fermi theory for modeling biological ion channels. J. Chem. Phys. 141 (22), 12B640_1.
Liu, W., 2009. One-dimensional steady-state poisson–nernst–planck systems for ion channels with multiple ion species. J. Differ. Equ. 246 (1), 428–451.
Magleby, K., Stevens, C., 1972. The effect of voltage on the time course of end-plate currents. J. Physiol. (Lond.) 223 (1), 151–171.
Malmivuo, J., Plonsey, R., 1995. Bioelectromagnetism: Principles and Applications of Bioelectric and Biomagnetic Fields. Oxford University Press, USA.
Markham, M.R., 2013. Electrocyte physiology: 50 years later. J. Exp. Biol. 216 (13), 2451–2458.
Mauro, A., 1969. The role of the voltaic pile in the galvani-volta controversy concerning animal vs. metallic electricity. J. Hist. Med. Allied Sci. 24 (2), 140–150.
Mitra, A., Cymes, G.D., Auerbach, A., 2005. Dynamics of the acetylcholine receptor pore at the gating transition state. Proc. Natl. Acad. Sci. 102 (42), 15069–15074.
Mori, Y., Liu, C., Eisenberg, R.S., 2011. A model of electrodiffusion and osmotic water flow and its energetic structure. Physica D 240 (22), 1835–1852.
Nelson, J.S., Grande, T.C., Wilson, M.V., 2016. Fishes of the World. John Wiley & Sons.
Noda, M., Shimizu, S., Tanabe, T., Takai, T., Kayano, T., Ikeda, T., Takahashi, H., Nakayama, H., Kanaoka, Y., Minamino, N., et al., 1984. Primary structure of electrophorus electricus sodium channel deduced from cdna sequence. Nature 312 (5990), 121.
Novotny, J.A., Jakobsson, E., 1996. Computational studies of ion-water flux coupling in the airway epithelium. i. construction of model. Am. J. Physiol.-Cell Physiol. 270 (6), C1751–C1763.
Nygren, A., Fiset, C., Firek, L., Clark, J., Lindblad, D., Clark, R., Giles, W., 1998. Mathematical model of an adult human atrial cell: the role of k+ currents in repolarization. Circ. Res. 82 (1), 63–81.
Pods, J., Schönke, J., Bastian, P., 2013. Electrodiffusion models of neurons and extracellular space using the poisson-nernst-planck equations-numerical simulation of the intra-and extracellular potential for an axon model. Biophys. J. 105 (1), 242–254.
Rubinstein, I., 1990. Electro-Diffusion of Ions. SIAM.
Sheridan, R.E., Lester, H.A., 1977. Rates and equilibria at the acetylcholine receptor of electrophorus electroplaques. a study of neurally evoked postsynaptic currents and of voltage-jump relaxations. J. Gen. Physiol. 70 (2), 187.
Song, Z., Cao, X., Horng, T.-L., Huang, H., 2019. Selectivity of the kcsa potassium channel: analysis and computation. Phys. Rev. E 100 (2), 022406.
Song, Z., Cao, X., Huang, H., 2018a. Electroneutral models for a multidimensional dynamic poisson-nernst-planck system. Phys. Rev. E 98 (3), 032404.
Song, Z., Cao, X., Huang, H., 2018b. Electroneutral models for dynamic poisson-nernst-planck systems. Phys. Rev. E 97 (1), 012411.
Xu, J., Lavan, D.A., 2008. Designing artificial cells to harness the biological ion concentration gradient. Nat. Nanotechnol. 3 (11), 666.